# Enhanced-absorption in Doppler-free spectroscopy of the Rb atom $D_1$ line with monochromatic light: application to laser frequency stabilization

Peter Yun<sup>0</sup>, <sup>1</sup>, \* Rodolphe Boudot<sup>0</sup>, <sup>2</sup> Qiang Hao<sup>0</sup>, <sup>1</sup> and Shougang Zhang<sup>1</sup>

<sup>1</sup>National Time Service Center, Chinese Academy of Sciences, 710600 Xi'an, People's Republic of China. <sup>2</sup>FEMTO-ST, CNRS, Université Franche-Comté, ENSMM, Besançon, France. (Dated: January 6, 2025)

The detection of narrow and high-amplitude optical resonances in atomic cells is of crucial importance for the development of compact and high-stability lasers or vapor cell optical references. In this work, using monochromatic light and proper polarization setting of the counter-propagating pump and probe beams, we demonstrate the detection of enhanced-absorption sub-Doppler resonances on the  $D_1$  line of Rb atom. We report a theoretical model showing that the Zeeman coherence induced between magnetic sub-levels, especially in the  $F \to F' = F - 1$  systems, with F and F' being the hyperfine quantum numbers of ground and excited states respectively, play a key role in the observed enhanced-absorption process. The theoretically predicted behaviour matches well the experimental observations. The impact of light polarization, laser intensity, magnetic field and cell temperature onto the Doppler-free resonance features is experimentally investigated. For application, two identical diode lasers were frequency-stabilized onto enhanced-absorption sub-Doppler resonances. The fractional frequency stability of the laser beatnote is measured to be  $1.8 \times 10^{-12}$  at 1 s and  $8.4 \times 10^{-12}$  at  $10^4$  s. These results demonstrate the interest of this scheme for the implementation of a compact or even chip-scale optical frequency reference, which might find applications in instrumentation, navigation and metrology.

#### I. INTRODUCTION

Sub-Doppler spectroscopy [1–3] in alkali-metal vapor cells is an elegant method to perform high-precision probing of atomic or molecular resonance spectral lines. Due to its relative simplicity and reliability, this technique is widely used for laser frequency stabilization and the development of optical frequency references.

A well-established spectroscopic approach used for the implementation of cell-based optical references relies on the excitation of the two-photon transition (TPT) of rubidium. Pioneerly studied in the 1990s [4–7], this technique has known a renewed interest over the last years [8–11] and has motivated several remarkable developments for various field-deployable applications [12–14]. Also, inspired by the success of microwave chip-scale atomic clocks (CSACs) [15–18], and by the rapid development of chip-scale optical frequency combs [19–22], some Rb two-photon clocks based on microfabricated vapor cells have been recently demonstrated with short-term fractional frequency stability at 1 s in the low 10<sup>-13</sup> range [23–26].

The optical  $D_1$  or  $D_2$  transition of alkali metal [27], with a natural linewidth of a few MHz, is also often used for laser frequency stabilization. Various Doppler-free spectroscopy schemes have been explored including saturated absorption spectroscopy (SAS) [28–32], polarization spectroscopy (PS) [33], or modulation transfer spectroscopy (MTS) [34]. The use of SAS with the  $D_2$  line of alkali atoms is quite popular. Rovera et al. demonstrated external-cavity diode lasers (ECDLs) stabilized

on the Cs  $D_2$  line with a fractional stability of  $4 \times 10^{-13}$  at 1 s [35]. An ultra-compact optical frequency reference, with a frequency stability of  $1.4 \times 10^{-12}$  at 1 s and below  $10^{-11}$  at  $10^5$  s, and dedicated to nanosatellites applications, was demonstrated in Refs [36, 37]. Sub-kilohertz laser linewidth narrowing was reported with polarization spectroscopy [38]. MTS, with the advantages of insensitivity to background absorption and rejection of low-frequency noise, has allowed the demonstration of lasers with a frequency stability at the level of a few  $10^{-13}$  at 1 s in Rb and Cs [39–41], and even down to the  $10^{-14}$  range using the  $D_2$  line of rubidium [42]. MTS has been also widely used for the development of high-stability molecular iodine cell clocks [43–45].

Dual-frequency sub-Doppler spectroscopy (DFSDS) was also reported [46–48]. In this approach, atoms in the vapor cell interact with two counter-propagating bichromatic laser fields. The destructive interference of Zeeman and hyperfine dark states, created by incident and reflected light fields, yields for the specific class of zero velocity atoms the detection of high-contrast enhanced-absorption sub-Doppler resonances. With this method, a Cs microcell-stabilized ECDL has achieved a stability of  $3\times10^{-13}$  at 1 s [49]. DFSDS was also explored with the Rb atom D<sub>1</sub> line [50].

In this work, we demonstrate, using proper light polarization setting in the counter-propagating pumpprobe scheme, the detection of sign-reversed enhancedabsorption Doppler-free resonances with high signal to linewidth ratio on the Rb  $D_1$  line. Such resonances reveal to be interesting candidates for laser frequency stabilization. In comparison with the DFSDS work reported in [46, 49], sub-Doppler resonances are here obtained using a single-frequency light-field, avoiding the necessity to microwave-modulate the laser (typically by using an

<sup>\*</sup> Corresponding author: yunenxue@ntsc.ac.cn, permanent e-mail: yunenxue@163.com

electro-optic modulator) and then simplifying the system architecture. The spectroscopic scheme studied here is obtained in the most basic retro-reflected configuration, without separating the pump and the probe beams. This prevents the addition of an optical modulator to modulate the pump beam as in MTS. Also, while TPT schemes require high laser intensities and cell temperatures (typically > 90 °C) for optimization of the reference short-term stability, the spectroscopic lines are here obtained for modest laser powers ( $\sim 100\,\mu\mathrm{W})$  and cell temperatures ( $\sim 40\,^{\circ}\mathrm{C}$ ). All these features are of significant interest for the demonstration of a high-performance and simple-architecture hot vapor cell optical reference.

A theoretical model is developed to understand qualitatively the phenomenon of enhanced-absorption in Doppler-free spectroscopy of Rb D<sub>1</sub> line and reveals the general features of experimental observations. Enhanced absorption, especially observed for the  $F \rightarrow F' = F - 1$  system (with F (F') the hyperfine quantum numbers of ground (excited) state), is mainly explained by Zeeman coherence and found to be, for the signal amplitude, maximized for intermediate polarization angles (0 <  $\theta$  < 90°) between the incident and reflected light fields. The influence of some key parameters onto the sub-Doppler resonances features is experimentally investigated. Using this simple-architecture setup, we demonstrate a laser beatnote with a fractional frequency stability of  $1.8 \times 10^{-12}$  at 1 s and below  $10^{-11}$  at  $10^4$  s.

#### II. THEORETICAL ANALYSIS

The investigated scheme consists on two counterpropagating linearly polarized pump and probe beams, interacting with a rubidium atomic ensemble in a vapor cell. We consider the simplified 5-level atomic system shown in Fig. 1. The proposed model aims to understand qualitatively the phenomenon of enhanced-absorption in Doppler-free spectroscopy of Rb  $D_1$  line, and to capture general features of sign-reversed sub-Doppler resonances experimentally observed in section III. The proposed model does not predict the quantitative evolution of the specific features (amplitude, linewidth) of the sub-Doppler resonances with key experimental parameters. For this purpose, an extended model should be developed, considering the full atomic system structure (11 Zeeman levels). This remains out of scope of the present work.

In the system shown in Fig. 1, we consider the case  $I_p < I_{sat}$ , with  $I_p$  the pump intensity and  $I_{sat}$  the saturation intensity. The electric field  $E_{pu}$  of the linearly polarized pump beam is:

$$\begin{aligned} \boldsymbol{E_{pu}} &= \mathcal{E}_1 cos(\omega_+ t - k_+ z) \hat{e}_x \\ &= \mathcal{E}_1 cos(\omega_+ t - k_+ z) (-\hat{e}_+ + \hat{e}_-) / \sqrt{2}, \end{aligned} \tag{1}$$

where  $\omega_{\pm}$  and  $k_{\pm}$  are the laser angular frequency and wave numbers of pump (probe) beams, seen by the atoms

with velocity v along the -z axis, respectively.  $\hat{e}_{x(y)}$  is the unit vector along x(y)-axis direction, and  $\hat{e}_{\pm} = \mp (\hat{e}_x \pm i\hat{e}_y)/\sqrt{2}$  is the spherical base of circular polarization.

With electric dipole approximation, the dark state  $|d_{pu}\rangle$  prepared by the pump beam is:

$$|d_{pu}\rangle = \cos\varphi |1\rangle - \sin\varphi |-1\rangle$$
  
=  $(|1\rangle + |-1\rangle)/\sqrt{2}$ , (2)

where  $\sin\varphi = \Omega_+/\sqrt{\Omega_+^2 + \Omega_-^2}$ ,  $\cos\varphi = \Omega_-/\sqrt{\Omega_+^2 + \Omega_-^2}$ , with  $\Omega_\pm = -\mathcal{E}_1\hat{e}_\pm d_{\mp 1e}/(\sqrt{2}\hbar) = \mp\Omega$  is the Rabi frequency with  $\Omega \in R$  (real number), in which  $d_{\mp 1e}$  is the electric dipole matrix element of each transition and  $\hbar$  is the reduced Planck constant.

The interaction Hamiltonian for the pump beam is then:

$$V_1 = -\mathbf{E}_{pu}\mathbf{D} = \hbar\Omega(|e\rangle\langle 1| - |e\rangle\langle -1|) + H.C., \tag{3}$$

with D the electric dipole operator, and H.C. denotes the Hermitian conjugate. Here, we can see that  $V_1 | d_{pu} \rangle = 0$ . A dark state is generated by the pump beam. Zeeman coherence and population trapping between  $|1\rangle$  and  $|-1\rangle$  are created.

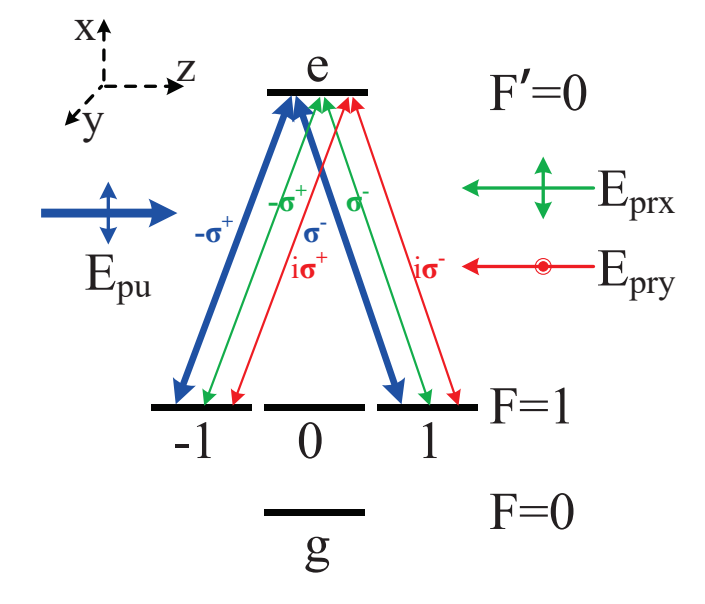


FIG. 1. Simplified 5-level atomic system that interacts with counter-propagated pump and probe beams, i.e., the transition with  $F=1 \rightarrow F'=0$ . We indicate Zeeman sublevels labeled by their magnetic quantum number  $m_F=-1,0,1$  in the ground state F=1. The states e and g stand for the sole Zeeman state in the excited state (with F'=0) and ground state (with F=0), respectively. The linear pump beam, as well as the two linearly orthogonal components of the probe beam, can be decomposed into two counter-rotating circular polarizations, respectively. Note that the quantization axis is chosen to be parallel with the direction of probe- or pump-beam propagation.

The electric field  $E_{pr}$  of the linearly polarized probe beam light, relative to x-axis with an angle  $\theta$ , can be written as:

$$\mathbf{E_{pr}} = \mathcal{E}_2 cos(\omega_- t + k_- z)(-e^{-i\theta}\hat{e}_+ + e^{i\theta}\hat{e}_-)/\sqrt{2}.$$
 (4)

When  $\theta = 0$ , i.e., for a x-axis polarized probe beam, denoted as the lin//lin case, the interaction Hamiltonian for the probe beam is:

$$V_{2x} = \hbar r \Omega(|e\rangle\langle 1| - |e\rangle\langle -1|) + H.C., \tag{5}$$

with  $r = \mathcal{E}_2/\mathcal{E}_1$ . In this case, we find that  $V_{2x} | d_{pu} \rangle = 0$ , meaning that  $| d_{pu} \rangle$  is also a dark state for the probe beam. Atoms are then uncoupled from the probe light, resulting in increased transmission of the probe light through the cell.

At the opposite, for the y-axis polarized probe beam  $(\theta = 90^{\circ}, \text{ lin} \perp \text{lin case})$ , the interaction Hamiltonian for the probe beam is given by:

$$V_{2y} = \hbar r \Omega(i|e\rangle\langle 1| + i|e\rangle\langle -1|) + H.C.$$
 (6)

This leads to  $V_{2y} | d_{pu} \rangle \neq 0$ , meaning that the  $| d_{pu} \rangle$  is not a dark state but a bright state for the probe beam. It results in increased absorption of the probe light.

In order to get a quantitative analysis for arbitrary linear polarization of the probe beam, and then predict the the resonance features observed in the following experiments, we use the Liouville equation. It provides the evolution of the density matrix for atoms at rest, based on the light-atom interaction system shown in Fig. 1. Details are deduced in the appendix. All the following theoretical results are obtained with the parameters: decay rate of the excited state  $\Gamma = 2\pi \times 5.75 \,\mathrm{MHz}$ , decay rate of the excited state's optical coherence  $\Gamma_c = \Gamma/2$ , Rabi frequency of the pump beam  $\Omega = 0.15 \Gamma$ , electric field amplitude ratio of probe to pump beam r = 0.5, temperature of atomic ensemble in the vapor cell  $T_{cell} = 40 \,^{\circ}\text{C}$ ,  $\gamma_1$  is a rate for the atomic system that leaves the experimental region,  $\gamma_c$  is the relaxation rate of the Zeeman coherence, i.e., the coherence decay rate between  $|1\rangle$  and  $|-1\rangle$ . Assuming a Gaussian laser beam with a  $1/e^2$  radius  $(R \sim 0.94 \,\mathrm{mm})$  passing through a dilute gas of atoms with a mean velocity  $u \sim 245\,\mathrm{m\,s^{-1}}$ , the transit rate of an atom through the beam is  $\gamma_1 = u/(2R) \approx 0.13 \,\mathrm{MHz}$ . We fixed  $\gamma_c = \gamma_1$  for simplification of the analysis. The detection time, that corresponds to the duration over which the signal is averaged for a given value of the laser frequency scan, was fixed a  $t = 10 \,\mu s$ . The results of numerical calculation are then plotted, i.e., the atomic population and coherence as shown in Fig. 10 and Fig. 11 in the appendix.

When the atomic optical coherences are averaged over the Maxwell-Boltzmann velocity distribution, absorption coefficients ( $\alpha_{\pm}$ ) and polarization rotation angle difference ( $\beta$ ) between the two counter-rotating circularly polarized components of the probe beam can be deduced (see Eq. A.11 to A.13 in the appendix). These terms are shown in Fig. 2, versus the laser detuning, for various polarization angles  $\theta$ .

In Fig. 2, Doppler-broadening absorption for both counter-rotating circularly polarized components of the probe beam is observed, for all  $\theta$ . Near the resonance, when  $\theta=0^{\circ}$  or  $90^{\circ}$ , enhanced-transmission or absorption signals appear due to the constructive or destructive interference of above mentioned processes. Note that in these two cases ( $\theta=0^{\circ}$  or  $90^{\circ}$ ), no dichroism or birefringence occurs ( $\alpha_{+}=\alpha_{-}$  and  $\beta=0$ ). At the opposite, when  $0<\theta<90^{\circ}$ , dichroism and birefringence appear. The transmission of the y-axis and x-axis polarized components of the probe beam is then related to both dichroism and birefringence terms values (see Eq. A.8 and Eq. A.11 to A.13).

Figure 3(a) shows the transmission of the y-axis polarized component of the probe beam, in cases where  $\theta = 90^{\circ}$ and  $\theta = 45^{\circ}$ , versus the laser detuning. At  $\theta = 45^{\circ}$ , the amplitude S of the sub-Doppler resonance is significantly increased. Figure 3(b) reports the absorption-enhanced Doppler-free dip's amplitude S, contrast C (defined as  $S/B_{DB}$ , with  $B_{DB}$  the bottom of the Doppler-broadened profile background), the background  $B_{DB}$  (with a normalization factor of 0.2), the imaginary part of the Zeeman coherence (with a normalization factor of 30), and a simple model prediction, versus the polarization angle  $\theta$ . The contrast C is decreased when the polarization angle is increased. The amplitude S of the sub-Doppler resonance reaches a maximum around  $\theta = 50^{\circ}$ . This behavior agrees well with our experiment observation (see Fig. 6(a)). As  $S = C \times B_{DB}$ , we also plot C and  $B_{DB}$  in the same figure. It indicates that the optimal angle for the maximum of S results from a compromise between the dark states fraction ratio and the probe beam's y-axis polarized component amplitude.

We have also developed a simple model, which assumes that the absorption-enhanced signal amplitude S is proportional to both the dark states fraction ratio and the electric field amplitude of the y-axis polarized component of probe beam, which destructive interferes with the generated dark states. The former, i.e., the fraction of dark states from the atomic ensemble, is proportional to the electric field amplitude of the x-axis polarized pump beam and the same polarized component of probe beam. Thus we get the relation  $S \propto (\mathcal{E}_1 + \mathcal{E}_2 cos\theta) \times \mathcal{E}_2 sin\theta$ , which is also shown as the purple curve in Fig. 3(b). This simple model qualitatively matches the numerical calculated signal amplitude S (red curve in Fig. 3(b)). This indicates that the process of dark states destructively interferes with the y-axis polarized component of the probe beam play a key role in maximizing the the signal amplitude of absorption-enhanced Doppler-free resonances. For reference, we also plot Zeeman coherence  $(\rho_{1,-1,i})$  in Fig. 3(b). Finally, we note that the contrast reaches its maximum around  $\theta = 0^{\circ}$ . Nevertheless, we chose the signal amplitude (S) as a reference parameter for our optical frequency reference application since the very low

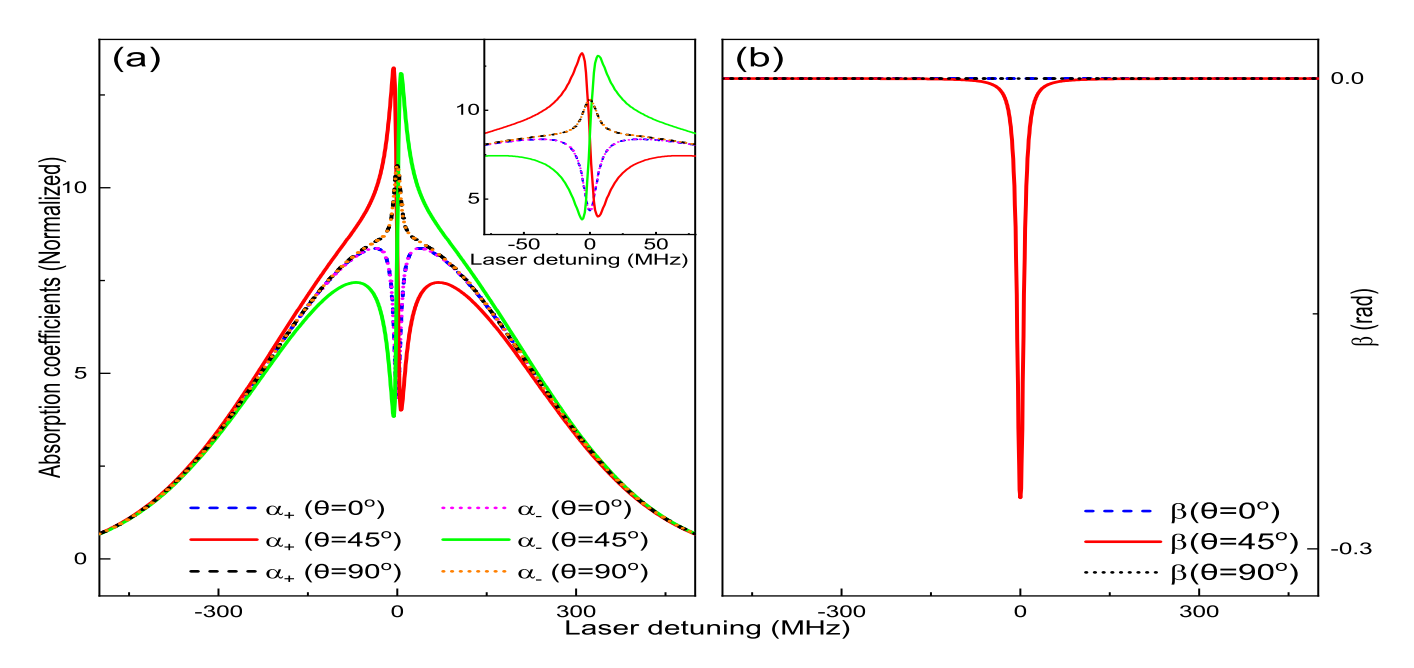


FIG. 2. Absorption coefficients (a), and polarization rotation angle difference (b) of the two counter-rotating circularly polarized components of the probe beam, versus the laser detuning, for various polarization angles. The inset in the top right of (a) shows the magnification of absorption coefficients near the resonance.

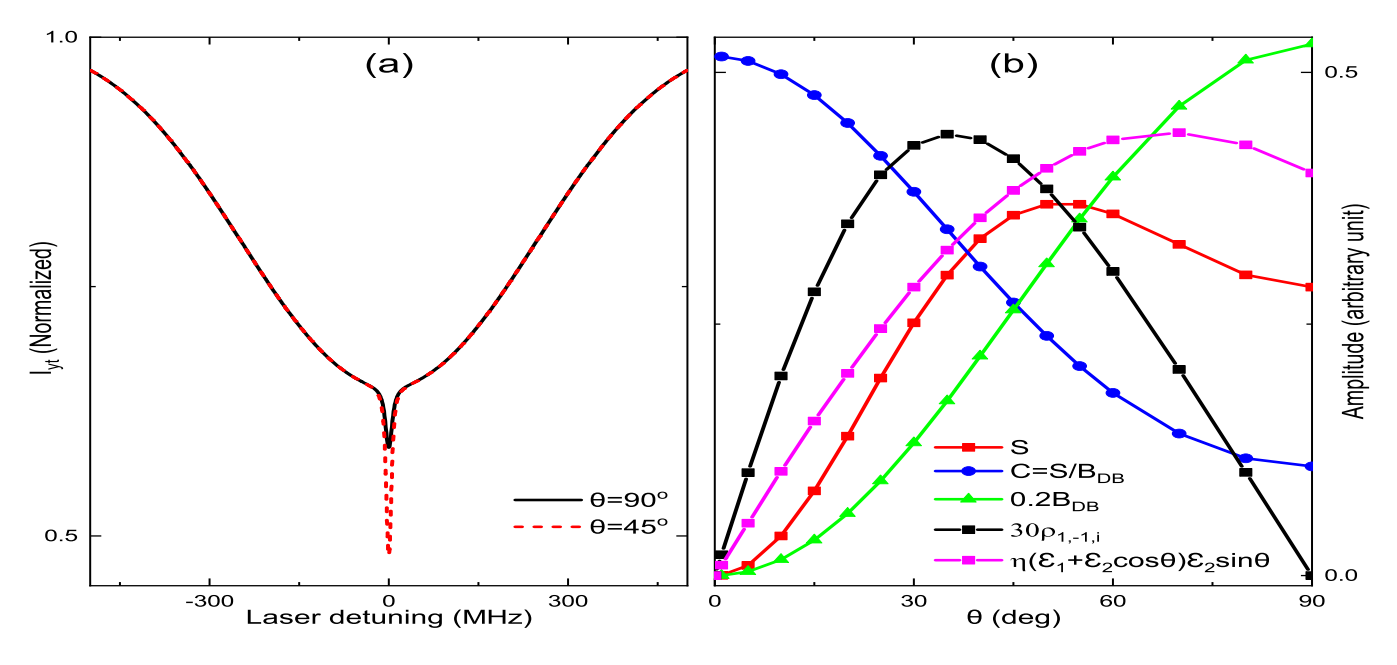


FIG. 3. (a) Theoretical calculated normalized-transmission of the y-axis polarization versus the laser detuning, for two polarization angles ( $\theta = 90$  or  $45^{\circ}$ ). (b) Signal amplitude (S) and contrast ( $C = S/B_{DB}$ ) of the absorption-enhanced Doppler-free dip, with  $B_{DB}$  the bottom of the Doppler-broadened profile, enlarged imaginary part of Zeeman coherence ( $\rho_{1,-1,i}$ ), and a simple model prediction:  $\eta(\mathcal{E}_1 + \mathcal{E}_2 cos\theta) \times \mathcal{E}_2 sin\theta$  ( $\eta$  is an arbitrary constant), versus the polarization angle  $\theta$ .

detected light power around  $\theta = 0^{\circ}$  would have led to a poor signal-to-noise ratio.

# III. EXPERIMENTAL SET-UP

Figure 4 depicts our experimental setup. A distributed Bragg Resonator (DBR) diode laser (Photodigm, PH795DBR), with a spectral linewidth of about 1 MHz, emits light at 795 nm. A 28 dB optical isolator (Iso, Thorlabs, IO-5-780-VLP) is placed at the output

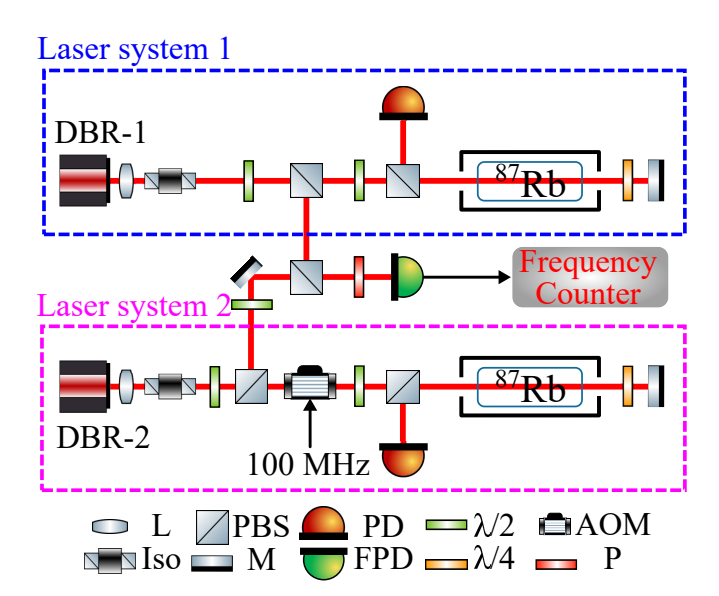


FIG. 4. Experimental setup for characterization of the DBR lasers, which are frequency-stabilized using Doppler-free spectroscopy with enhanced absorption in D<sub>1</sub> line of <sup>87</sup>Rb. L, lens; Iso, optical isolator; PBS, polarizing beam splitter; M, mirror; PD, photodetector; FPD, fast photodetector;  $\lambda/2$ , half-wave plate;  $\lambda/4$ , quarter-wave plate; AOM, acousto-optic modulator; P, polarizer.

of the laser to prevent spurious feedback. A polarizing beam splitter (PBS), preceded by a half-wave plate, is placed to extract a fraction the laser power at the isolator output. The laser beam, incident in the vapor cell, is then used as the pump beam. After interacting with the atomic vapor, the laser beam is retro-reflected by a mirror to produce the counter-propagating probe beam, which is overlapped with the pump beam. The polarization of the reflected probe beam can be adjusted using a quarter-wave plate inserted between the cell and the reflection mirror. The transmission of the probe beam is monitored at the cell input through the use of a PBS and a photodiode (PD, Thorlabs, PDA36A2). The gain of the photodiode is set to 40 dB for all following experiments except for the laser beatnote stability measurement (Figure 9) where a gain of 20 dB was used to increase the detection bandwidth.

The laser beam is elliptical, with a  $1/e^2$  diameter of about 2.1 mm and 1.7 mm. The  $^{87}{\rm Rb}$ -isotope-enriched cylindrical vapor cell has a diameter of 20 mm and a length of 50 mm. It is temperature stabilized at around  $40\,^{\circ}{\rm C}$ , except for the cell temperature tests reported in Fig. 8. The cell is surrounded by one layer of mu-metal magnetic shield. As shown in Figure 12 in the appendix, the maximum of enhanced-absorption signal amplitude is reached at null magnetic field.

Two quasi-identical laser setups, each frequency-stabilized to the absorption enhanced Doppler-free resonance, were implemented. For one of the them (Laser system 2 in Fig. 4), an acousto-optic modulator (AOM), driven by a 100 MHz radiofrequency signal, was im-

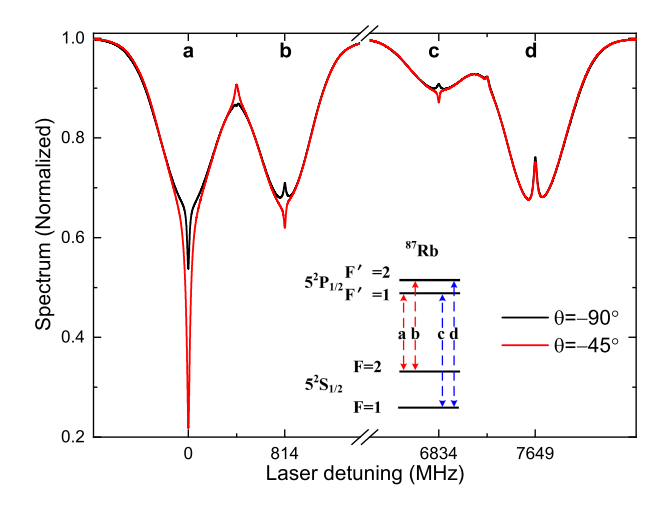


FIG. 5. Spectroscopic signals obtained with different polarization angles ( $\theta = -90^{\circ}$  and  $\theta = -45^{\circ}$ ) between the pump and the probe beams. Experimental parameters are:  $T_{cell} = 40 \,^{\circ}\text{C}$ ,  $P_{pump} = 100 \, \mu\text{W}$ ,  $B_0 = 0 \, \mu\text{T}$ . The inset shows the atomic levels involved in the  $D_1$  line of  $^{87}\text{Rb}$  atom with four transition lines noted 'a' to 'd'. These resonances are from left to right 'a':  $F = 2 \rightarrow F' = 1$ , 'b':  $F = 2 \rightarrow F' = 2$ , 'c':  $F = 1 \rightarrow F' = 1$ , 'd':  $F = 1 \rightarrow F' = 2$ .

plemented to shift the laser frequency. This allows, through superposition of both laser beams, to produce a  $100\,\mathrm{MHz}$  beatnote between the two laser setups. The beatnote is detected by a fast photodiode (FPD, Thorlabs, PDA10A2) and analyzed with a frequency counter (Keysight,  $53230\mathrm{A}$ ), referenced to an active hydrogen maser.

#### IV. EXPERIMENTAL RESULTS

#### A. Doppler-free spectrum

Figure 5 reports the measured Doppler-free spectra. In the  $lin \perp lin$  case ( $\theta = -90^{\circ}$ ), resonances noted 'b', 'c' and 'd' appear as transmission-enhanced peaks whereas the 'a' resonance is sign-reversed (enhanced absorption). with a contrast C of 18.1%. In the case where  $\theta = -45^{\circ}$ , resonances 'b' and 'c' are also reversed (enhanced absorption). The 'a' resonance, broadened to 32.7 MHz, instead of 21.7 MHz in the  $lin \perp lin$  case, appears as enhanced absorption and exhibits a much higher contrast of 66.9%, which is qualitatively agree with theoretical predictions of Figure 3(a). In the following, we have utilized the sub-Doppler resonance signal S, linewidth (FWHM) and corresponding signal/linewidth ratio (S/FWHM) for evaluating the impact of some key experimental parameters onto the Doppler-free resonance. The ratio S/FWHMcan be used as a figure of merit for optimization of the optical reference short-term stability [52]. In the following figures, the positive or negative value of the signal S stands for enhanced absorption or transmission of the

resonance, respectively.

# B. Polarization angle $(\theta)$

The effect of the polarization angle  $(\theta)$  on the characteristics of 'a' and 'b' spectral lines is shown in Fig. 6.

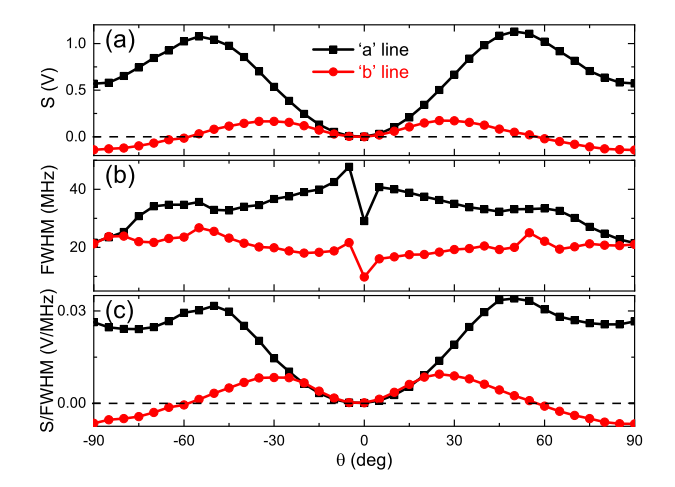


FIG. 6. Signal (a), linewidth (b) and S/FWHM ratio (c) of 'a' and 'b' lines versus the polarization angle  $\theta$ . Experimental parameters are:  $T_{cell} = 40\,^{\circ}\text{C}$ ,  $P_{pump} = 100\,\mu\text{W}$ ,  $B_0 = 0\,\mu\text{T}$ . The lines simply connect experimental data points to guide the eyes of the reader. The same applies hereinafter.

The amplitude S of the 'a' resonance, shown in Fig. 6(a), reaches a maximum for  $|\theta| \approx 52.5^{\circ}$  and is minimized for  $\theta = 0^{\circ}$ . This observed dependence qualitatively agrees with theoretical predictions of Fig. 3(b), i.e., both the signal amplitude (red curve) obtained with the Liouville equation and those based on a simpler model prediction (purple curve). The trend of the 'b' resonance signal versus  $\theta$  is similar, but with a different maximum location ( $\theta \approx \pm 27.5^{\circ}$ ) and a lower amplitude. The resonance linewidth, plotted in Fig. 6(b), changes discontinuously at  $\theta = 0^{\circ}$ . Even if very low light power is detected at this polarization angle, enhanced-absorption sub-Doppler dips are still observed for 'a' and 'b' resonances. The linewidth of the 'b' resonance also changes discontinuously for  $|\theta| \approx 60^{\circ}$ . This occurs at the angle where the resonance sign reverses, as illustrated by the zero-crossing of the signal on Fig. 6(a).

The S/FWHM ratio, shown in Fig. 6(c), reaches a maximum around  $\mid \theta \mid \approx 45^\circ$  and  $\mid \theta \mid \approx 25^\circ$  for 'a' and 'b' resonances, respectively. For completeness, we have also studied the spectral features of 'c' and 'd' resonances. We measured that these lines exhibited a smaller S/FWHM ratio than the 'a' and 'b' resonances. We chose then to focus on 'a' and 'b' resonances for the following experiments.

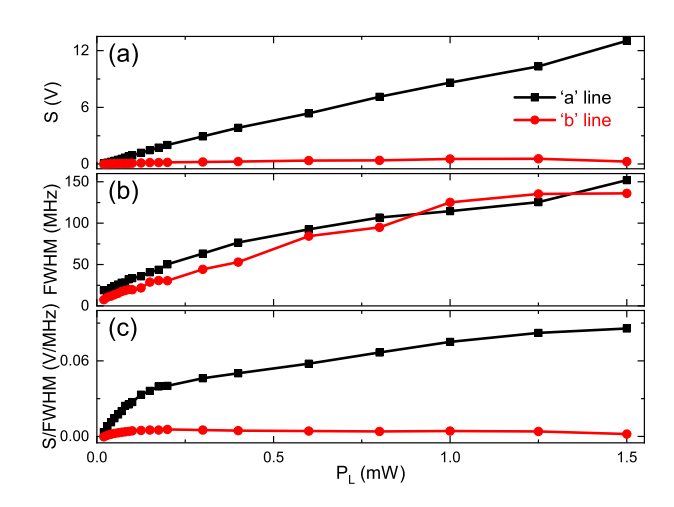


FIG. 7. Signal (a), linewidth (b) and S/FWHM ratio (c) of 'a' and 'b' lines versus the laser pump beam power. Experimental parameters are:  $T_{cell} = 40\,^{\circ}\text{C}$ ,  $\theta = -45\,^{\circ}$ ,  $B_0 = 0\,\mu\text{T}$ .

#### C. Pump beam power

Figure 7 summarizes the effect of the pump beam laser power  $P_L$  on the Doppler-free 'a' and 'b' resonances.

For the 'a' resonance, the signal height S is increased with the laser beam power in the investigated power range. For the 'b' resonance, the signal height S is increased much more slowly, tends to reach its maximum for  $P_L \approx 1.25\,\mathrm{mW}$ , and then starts to go down. For both lines, the linewidth of the sub-Doppler resonance is increased with  $P_L$ . Shown in Fig. 7(c), the slope of S/FWHM ratio of the 'a' resonance is reduced for power values higher than about 200 µW. In the case of the 'b' resonance, the S/FWHM ratio reaches its maximum around 200 µW.

### D. Cell temperature

The effect of the cell temperature  $T_{cell}$  on the 'a' and 'b' Doppler-free resonances is shown in Fig. 8. The maximum signal height of 'a' and 'b' resonances is reached for  $T_{cell}=41\,^{\circ}\mathrm{C}$  and  $48\,^{\circ}\mathrm{C}$ , respectively. For the 'a' resonance, the linewidth increases firstly with the cell temperature and starts to decrease for  $T_{cell}$  higher than  $52\,^{\circ}\mathrm{C}$ . For the 'b' resonance, the linewidth starts to decrease after  $T_{cell}\approx28\,^{\circ}\mathrm{C}$ . The maximum S/FWHM ratio of 'a' and 'b' resonances is reached for  $T_{cell}\approx40\,^{\circ}\mathrm{C}$  and  $52\,^{\circ}\mathrm{C}$ , respectively. From the experimental investigation reported above, we find that the maximum S/FWHM ratio is much higher for the 'a' resonance. We decided then to use this resonance to implement laser frequency stabilization tests.

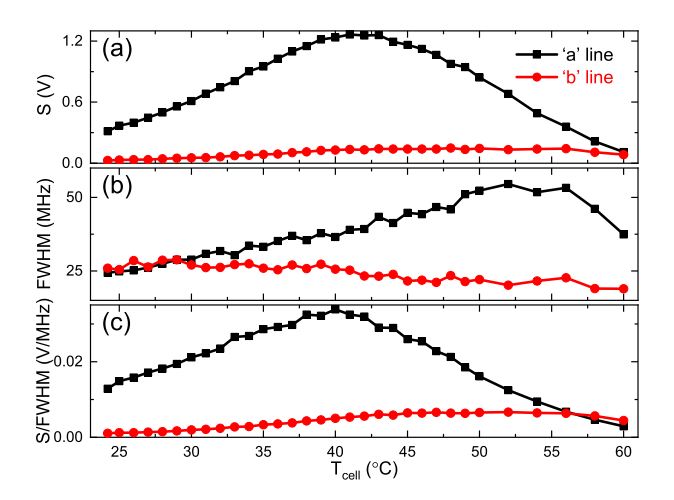


FIG. 8. Signal (a), linewidth (b) and S/FWHM ratio (c) of 'a' and 'b' lines versus the cell temperature  $T_{cell}$ . Experimental parameters are:  $P_{pump}=100\,\mu\text{W},\,\theta=-45^\circ,\,B_0=0\,\mu\text{T}.$ 

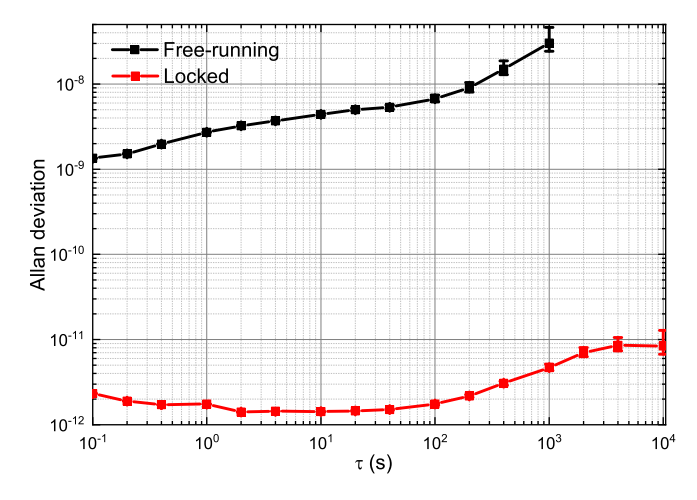


FIG. 9. All an deviation of the laser beatnote frequency in the free-running (black) and locked (red) regimes. Experimental parameters are:  $T_{cell}=40\,^{\circ}\mathrm{C},\ P_{pump}=100\,\mathrm{\mu W},\ \theta=-45^{\circ},\ B_{0}=0\,\mathrm{\mu T}.$ 

# E. Allan deviation of the laser beatnote

In a last part, we have performed frequency stability measurements of the laser beatnote between both laser systems. Each laser is frequency stabilized onto the 'a' resonance. For this purpose, an error signal is derived from the spectroscopic signal at the photodiode output using synchronous modulation-demodulation technique, operating at a modulation frequency  $f_M=200\,$  kHz. Thanks to a proportional-integral (PI) controller (Vescent, D2-125-PL), the error signal is fed back to the laser dc current with a bandwidth of about 100 kHz, for stabilization of the laser frequency onto the atomic resonance. Frequency stability results, in the free-running and locked regimes, are reported in Fig. 9.

In the free-running regime, the laser beatnote frac-

tional frequency stability is  $2.7 \times 10^{-9}$  at 1s and is degraded for longer integration times to reach  $3 \times 10^{-8}$  at 10<sup>3</sup> s. In the locked case, where both lasers are stabilized to the absorption-enhanced Doppler-free signal, the Allan deviation of the laser beatnote is improved by more than 3 orders of magnitude, yielding  $1.8 \times 10^{-12}$  at 1s and  $8.4 \times 10^{-12}$  at  $10^4$  s. Performances at 1 s, obtained here for a single-frequency laser setup, are comparable to those obtained in [52] using DFSDS. For  $\tau > 10^2$  s, the degradation of the frequency stability is not quantitatively explained to date. The sensitivity of the optical reference frequency to variations of laser power or cell temperature, as well as typical fluctuations of these experimental parameters, will be measured in the future to estimate their contributions onto the reference long-term stability.

#### V. CONCLUSIONS

Through optimized polarization setting of the counterpropagating pump-probe configuration, we have demonstrated enhanced-absorption Doppler-free spectroscopy on the  $D_1$  line of Rb atom at 795 nm. We have reported a theoretical model that shows the important contribution of Zeeman dark states in this spectroscopic scheme. The impact of several key parameters on the sub-Doppler resonance features was investigated experimentally. In a last part, we have stabilized two quasi-identical laser systems using this spectroscopic approach. The Allan deviation of the laser beatnote is in the locked regime  $1.8 \times 10^{-12}$  at 1s and below  $10^{-11}$  at  $10^4$  s. These results demonstrate the interest of this approach for the implementation of a compact and high-stability vapor cell optical frequency reference.

#### **ACKNOWLEDGEMENTS**

We gratefully acknowledge Ms. Candy Xiong (NTSC) for thoroughly reading and polishing our manuscript. This work was funded by the National Key R&D Program of China (2023YFC2205400) and National Natural Science Foundation of China (Grant No. 12173043, Grant No. U1731132). This work was partly funded by Centre National d'Etudes Spatiales (CNES) in the frame of the OSCAR project (Grant 200837/00). This work was also supported by the Agence Nationale de la Recherche (ANR) in the frame of the LabeX FIRST-TF (Grant ANR 10-LABX-48-01), the EquipX Oscillator-IMP (Grant ANR 11-EQPX-0033) and the EIPHI Graduate school (Grant ANR-17-EURE-0002) through the REMICS project.

#### AUTHOR DECLARATIONS

#### Conflict of Interest

The authors have no conflicts to disclose.

# **Author Contributions**

Peter Yun: Conceptualization (lead); Theoretical model development (led); Methodology (led); Experimental realization (led); Data curation (led); Formal analysis (led); Validation (lead); Writing-original draft (lead). Rodolphe Boudot: Writing-original draft (supporting); Writing-Reviewing and Editing (led); Formal analysis (supporting); Validation (supporting). Qiang Hao: Physics package design and mount (supporting); Software (lead); Writing-Reviewing and Editing (supporting). Shougang Zhang: Writing-Reviewing and Editing (supporting); Resources (lead).

#### DATA AVAILABILITY

The data that support the findings of this study are available from the corresponding author upon reasonable request.

### APPENDIX A: THEORETICAL SIMULATION

In this section, we show the importance of Zeeman coherence in the process of absorption-enhanced Doppler-free spectroscopy. This study is extracted from theoretical simulations based on the 5-level model shown in Fig. 1, using the Liouville equation and the polarization rotation calculation method.

### 1. Liouville equations

The evolution of the density matrix for atoms at rest is given by the Liouville equation. Without relaxation terms at first, it reads:

$$\dot{\rho} = \frac{-i}{\hbar}[H, \rho],\tag{A.1}$$

where  $H = H_0 + V$ ,  $H_0 = \hbar \omega_e$  is the Hamiltonian of the unperturbed atom, and  $\omega_e$  is the angular frequency for the level  $|e\rangle$ . The interaction Hamiltonian, induced by the pump beam, and x- and y-axis polarized components of the probe beam respectively, is  $V = V_1 + V_{2x} + V_{2y}$ .

With electric dipole approximation, the Hamiltonian is:

$$H = \hbar \begin{bmatrix} 0 & 0 & 0 & a \\ 0 & 0 & 0 & 0 \\ 0 & 0 & 0 & -a* \\ a & 0 & -a & \omega_e \end{bmatrix}, \tag{A.2}$$

with  $a = \Omega \cos(\omega_+ t) + r\Omega e^{i\theta} \cos(\omega_- t)$ .

The Liouville equations with interested atomic levels can thus be written as:

$$\begin{split} \dot{\rho}_{1,1} &= -2Im(a^*\rho_{1,e}), \\ \dot{\rho}_{-1,-1} &= 2Im(a\rho_{-1,e}), \\ \dot{\rho}_{e,e} &= 2Im(a^*\rho_{1,e}) - 2Im(a\rho_{-1,e}), \\ \dot{\rho}_{1,-1} &= -ia(\rho_{-1,e}^* + \rho_{1,e}), \\ \dot{\rho}_{1,e} &= i[a(\rho_{1,1} - \rho_{e,e}) - a^*\rho_{1,-1} + \rho_{1,e}\omega_e], \\ \dot{\rho}_{-1,e} &= i[a^*(\rho_{e,e} - \rho_{-1,-1}) + a\rho_{1,-1}^* + \rho_{-1,e}\omega_e]. \end{split}$$
(A.3)

In order to calculate the atomic population and coherence, we transform the density matrix equation with slowly variables, as defined by [53], such as:  $\rho_{1,e} = \sigma_{1,e+}e^{i\omega_+t} + \sigma_{1,e-}e^{i\omega_-t}, \; \rho_{-1,e} = \sigma_{-1,e+}e^{i\omega_+t} + \sigma_{-1,e-}e^{i\omega_-t}.$ 

Under the rotating wave approximation, and considering the relaxation terms into consideration, we arrive to:

$$\begin{split} \dot{\rho}_{1,1} &= -\Omega(\sigma_{1,e+,i} - r\sin\theta\sigma_{1,e-,r} + \cos\theta\sigma_{1,e-,i}) + \rho_{e,e}\Gamma/4 - \rho_{1,1}\gamma_{1} + \gamma_{1}/4, \\ \dot{\rho}_{-1,-1} &= \Omega(\sigma_{-1,e+,i} + r\sin\theta\sigma_{-1,e-,r} + \cos\theta\sigma_{-1,e-,i}) + \rho_{e,e}\Gamma/4 - \rho_{-1,-1}\gamma_{1} + \gamma_{1}/4, \\ \dot{\rho}_{e,e} &= \Omega(\sigma_{1,e+,i} - r\sin\theta\sigma_{1,e-,r} + \cos\theta\sigma_{1,e-,i}) - \Omega(\sigma_{-1,e+,i} + r\sin\theta\sigma_{-1,e-,r} + \cos\theta\sigma_{-1,e-,i}) - \rho_{e,e}(\Gamma + \gamma_{1}), \\ \dot{\rho}_{1,-1} &= -\gamma_{c}\rho_{1,-1} - i\Omega[\sigma_{-1,e+}^{*} + \sigma_{1,e+} + re^{i\theta}(\sigma_{-1,e-}^{*} + \sigma_{1,e-})]/2, \\ \dot{\sigma}_{1,e+} &= (-i\Delta_{+} - \Gamma_{c} - \gamma_{1})\sigma_{1,e+} - i\Omega(\rho_{e,e} - \rho_{1,1} + \rho_{1,-1})/2, \\ \dot{\sigma}_{1,e-} &= (-i\Delta_{-} - \Gamma_{c} - \gamma_{1})\sigma_{1,e-} - ir\Omega[e^{i\theta}(\rho_{e,e} - \rho_{1,1}) + e^{-i\theta}\rho_{1,-1}]/2, \\ \dot{\sigma}_{-1,e+} &= (-i\Delta_{-} - \Gamma_{c} - \gamma_{1})\sigma_{-1,e+} + i\Omega(\rho_{e,e} - \rho_{-1,-1} + \rho_{1,-1}^{*})/2, \\ \dot{\sigma}_{-1,e-} &= (-i\Delta_{-} - \Gamma_{c} - \gamma_{1})\sigma_{-1,e-} + ir\Omega[e^{-i\theta}(\rho_{e,e} - \rho_{-1,-1}) + e^{i\theta}\rho_{1,-1}^{*}]/2, \end{split}$$

$$(A.4)$$

in which  $\sigma_{m,n,r(i)}$  is the real (imaginary) part of  $\sigma_{m,n}$ , with m,n  $\in$  ( $\pm 1, e \pm$ ), and we used:  $\Delta_{\pm} = \omega_{\pm} - \omega_{e} =$  $\omega \pm kv - \omega_e$ , here  $\omega$  and  $k = \omega/c$  are the laser angular frequency and wave number seen by the atoms with zero velocity along the -z axis, respectively. The initial conditions are:  $\rho_{-1,-1}(t=0) = \rho_{0,0}(t=0) = \rho_{1,1}(t=0)$  $0) = \rho_{q,q}(t = 0) = 0.25, \ \rho_{e,e}(t = 0) = \rho_{1,-1}(t = 0)$  $0) = \sigma_{1,e+}(t=0) = \sigma_{1,e-}(t=0) = \sigma_{-1,e+}(t=0) =$  $\sigma_{-1.e-}(t=0)=0.$ 

### Susceptibilities of the atomic medium

With the help of the Jones matrix, the electric field of the probe beam can be also written as:

$$\boldsymbol{E_{pr}} = \frac{\mathcal{E}_2}{2} \left\{ -e^{-i\theta} \begin{bmatrix} -1 \\ -i \end{bmatrix} + e^{i\theta} \begin{bmatrix} 1 \\ -i \end{bmatrix} \right\}. \tag{A.5}$$

From Ref. [54], the probe beam, transmitted across the clock cell with length L, is changed to:

$$E_{prt} = \frac{\mathcal{E}_0}{2} \left\{ -e^{-i\theta + \xi_+} \begin{bmatrix} -1 \\ -i \end{bmatrix} + e^{i\theta + \xi_-} \begin{bmatrix} 1 \\ -i \end{bmatrix} \right\}$$
 (A.6)

where  $\xi_{\pm} = -i\beta_{\pm} - \alpha_{\pm}L/2$ ,  $\beta_{\pm} = 2\pi L n_{\pm}/\lambda$ ,  $n_{\pm}$  are the refractive indices of the <sup>87</sup>Rb atomic medium for the components that are left and right circularly polarized,  $\alpha_{+}$  are the corresponding absorption coefficients, and  $\lambda$ is the average wavelength of pump and probe beams.

For the y-axis polarized transmission light detection, we get:

$$I_{yt} = \varepsilon_0 \mathbf{E_{prty}} * \mathbf{E_{prty}^*}$$
  
=  $I_0[e^{-\alpha_+ L} + e^{-\alpha_- L} - 2e^{-\alpha L} \cos(2\theta + \beta)]/4$ , (A.7)

where  $I_0 = \varepsilon_0 \mathcal{E}_2^2$ ,  $\alpha = (\alpha_+ + \alpha_-)/2$ ,  $n_{\pm} \approx 1 + Re(\chi_{\pm})/2$ ,  $\alpha_{\pm} = 2\pi Im(\chi_{\pm})/\lambda$ , and  $\beta = \beta_{+} - \beta_{-}$ . As the y-axis polarized input light is  $I_{y_{in}} = I_0 \sin^2 \theta$ , the normalized

$$I_{ytN} = [e^{-\alpha_{+}L} + e^{-\alpha_{-}L} - 2e^{-\alpha L}\cos(2\theta + \beta)]/(4\sin^{2}\theta).$$
(A.8)

Then, we need to calculate the susceptibility. For atoms at rest, it can be written as:

$$\chi_{+} = \frac{-3N\lambda^{3}\Gamma}{4\pi^{2}} \left(\frac{\sigma_{-1,e^{-}}}{-e^{-i\theta}r\Omega}\right)^{*},$$

$$\chi_{-} = \frac{-3N\lambda^{3}\Gamma}{4\pi^{2}} \left(\frac{\sigma_{1,e^{-}}}{e^{i\theta}r\Omega}\right)^{*}.$$
(A.9)

with N the atomic density. Note that there is a slight difference from ref [55], the new definition expanded the original definition, i.e., we use  $\chi = \frac{-3N\lambda^3\Gamma}{4\pi^2} \left(\frac{\sigma_{g,e}}{\Omega}\right)^*$  rather than  $\chi = \frac{-3N\lambda^3\Gamma}{4\pi^2} \frac{\sigma_{g,e}^*}{\Omega}$ .

With averaging over the Maxwell-Boltzmann velocity distribution and using  $\Delta_{\pm} = \Delta \pm kv$ ,  $\chi_{+}$  is given by:

$$\chi_{+} = \frac{-3N\lambda^{3}\Gamma}{4\pi^{2}} \int_{-\infty}^{\infty} e^{-(\nu/u)^{2}} \left(\frac{\sigma_{-1,e-}}{-e^{-i\theta}r\Omega}\right)^{*} d\nu, (A.10)$$

where  $u = (2k_BT_{cell}/M)^{1/2}$  is the most probable velocity with M the mass of a  $^{87}$ Rb atom and  $k_B$  the Boltzmann constant. The absorption coefficient for  $\sigma_+$  light can be written as:

$$\alpha_{+} = A \int_{-\infty}^{\infty} e^{-(\nu/u)^{2}} (-\sigma_{-1,e-,r} \sin \theta - \sigma_{-1,e-,i} \cos \theta) d\nu,$$
(A.11)

where  $A = \frac{3N\lambda^2\Gamma}{2ur\Omega\pi^{3/2}}$ . Similarly, the absorption coefficient for  $\sigma_-$  light can be written as:

$$\alpha_{-} = A \int_{-\infty}^{\infty} e^{-(\nu/u)^{2}} (-\sigma_{1,e-,r} \sin \theta + \sigma_{1,e-,i} \cos \theta) d\nu,$$
(A.12)

We get also the polarization rotation angle difference  $(\beta)$  between the two counter-rotating circularly polarized components of the probe beam:

$$\beta = \frac{LA}{2} \int_{-\infty}^{\infty} e^{-(\nu/u)^2} (\sigma_{-1,e-,r} \cos \theta - \sigma_{-1,e-,i} \sin \theta + \sigma_{1,e-,r} \cos \theta + \sigma_{1,e-,i} \sin \theta) d\nu.$$
(A.13)

By inserting the numerical calculated results from Eq. A.4 into Eq. A.11 to A.13, and then Eq. A.8, we finally get the transmission spectroscopy of the y-axis polarized component of probe beam.

# 3. Theoretical results: Atomic Population, coherence and susceptibilities

Here we present partial of theoretical calculation results, i.e., atomic population and coherence for atoms at rest, which are not only necessary for calculating the absorption coefficients and polarization rotation angle, but also show the system's evolution under the interaction of pump-probe beam for zero velocity atom.

Figure 10 shows atomic populations  $(\rho_{1,1} \text{ and } \rho_{e,e})$  in (a), Zeeman coherence  $(\rho_{1,-1,r} \text{ and } \rho_{1,-1,i})$  in (b), and the probe beam felt slowly variable optical coherence  $(\sigma_{1,e-,r}, \sigma_{1,e-,i}, \sigma_{-1,e-,r} \text{ and } \sigma_{-1,e-,i})$  in (c and d) versus the laser detuning, for various polarization angles  $\theta$ , for zero velocity atoms.

At resonance (null laser detuning,  $\Delta_{+} = \Delta_{-} = 0$ , with  $\Delta_{+}$  and  $\Delta_{-}$  the laser detuning for the incident pump and reflected probe beams, respectively), the atomic population  $\rho_{1,1}(=\rho_{-1,-1})$  and the real part of the Zeeman coherence  $\rho_{1,-1,r}$  decrease when the polarization angle  $(\theta)$  is increased. The opposite behavior is observed for  $\rho_{e,e}$ . This can be explained by the fact that, with a weak pump intensity ( $I_p < I_{sat}$ ), optical pumping induced Zeeman coherence in ground states is more pronounced than the saturation effect and the population pumping effect between two set of ground hyperfine states (from F to F-1).

To be specific, when  $\theta = 0$ , the dark state prepared by the pump beam is also decoupled from the probe beam. A common dark state is then obtained for both beams such that, at resonance, the ground atomic population  $\rho_{1,1}(\rho_{-1,-1})$  and the real part of the Zeeman coherence  $\rho_{1,-1r}$  (relative to the transmission) reach their maximum. At the opposite, at  $\theta = 90^{\circ}$ , the dark state created by the pump beam is a bright state for the probe beam. In this case, there is no common dark state anymore. A decrease of the  $\rho_{1,1}(\rho_{-1,-1})$  and transmission  $(\rho_{1,-1,r})$ , and increase of  $\rho_{e,e}$ , is then observed. Interestingly, the situation is between these two cases for  $0 < \theta < 90^{\circ}$ . In this case, the resonance features results from a competition between the above-mentioned processes. As seen on Fig. 10(b), the imaginary part of the Zeeman coherence  $(\rho_{1,-1,i})$ , but also its real part  $(\rho_{1,-1,r})$ , exhibit two

bumps (maxima), when the laser frequency detuning is scanned, for  $\theta=45^{\circ}$ .

Figure 11 focuses on the evolution of the atomic populations (a), the probe beam felt optical coherence (b) and the Zeeman coherence (c) versus the polarisation angle  $\theta$ , for zero-velocity atoms and null laser detunings.

Figure 11(a) shows that, when  $\theta$  increases, atomic population trapping in the  $\rho_{1,1}(\rho_{-1,-1})$  is decreased, and the excited state  $\rho_{e,e}$  is increased. The atomic populations of  $\rho_{0,0}$  and  $\rho_{g,g}$ , which are proportion to  $\rho_{e,e}$ , also increase with  $\theta$ . The coherent population trapping effect becomes weak due the transformation from constructive (lin//lin) to destructive (lin $\perp$ lin) interference. During this process, we can find that the optical pumping induced population leak to non-resonant hyperfine ground states (F to F-1) plays a negative effect for the enhanced-absorption Doppler-free signal as  $\theta$  increases.

Figure 11(b) shows the imaginary and real part of the optical coherence seen by the two counter-rotating circularly-polarized components of the probe beam. The optical dichroism and birefringence are easier to read with the definitions  $\alpha_0$  and  $\beta_0$  given in Eq. A.11 to A.13, but without velocity averaging, i.e.,

$$\alpha_{0} = g_{1}(-\sigma_{-1,e-,r}\sin\theta - \sigma_{-1,e-,i}\cos\theta - \sigma_{1,e-,r}\sin\theta + \sigma_{1,e-,i}\cos\theta),$$

$$\beta_{0} = g_{2}(\sigma_{-1,e-,r}\cos\theta - \sigma_{-1,e-,i}\sin\theta + \sigma_{1,e-,r}\cos\theta + \sigma_{1,e-,i}\sin\theta),$$
(A.14)

with  $g_1$  and  $g_2$  arbitrary constant. We plotted  $\alpha_0$  and  $\beta_0$  in Figure 11(c), These parameters qualitatively agree with real  $(\rho_{1,-1,r})$  and imaginary  $(\rho_{1,-1,i})$  part of the Zeeman coherence shown in the same figure, respectively. The imaginary part of the Zeeman coherence  $(\rho_{1,-1,i})$  reaches its maximum around  $\theta=35^\circ$ . This behavior agrees with the observed maximum of the absorption-enhanced Doppler-free signal at intermediate angle in Figure 6(a).

# APPENDIX B: THE EFFECT OF STATIC MAGNETIC FIELD

In this part, the impact of the z-axis direction static magnetic field generated by a coil in the magnetic shield onto the features of 'a' and 'b' resonances are measured and reported in Figure 12.

For both resonances, the signal height S and the  $S/{\rm FWHM}$  ratio are maximized at null magnetic field. Such a behaviour was also observed in [47]. At higher static magnetic field, the enhanced absorption reverses to enhanced transmission around  $B_0 \approx 43\,\mu{\rm T}$  for the 'a' resonance, and  $6\,\mu{\rm T}$  for the 'b' resonance. For even higher values of  $B_0$ , we have observed that the enhanced transmission peak was reversed again to appear again as an enhanced absorption dip for the 'a' resonance. This

phenomenon might be due to the effect of light pressure discussed and observed in Ref. [51]. According to results obtained in Fig. 12, the other experiments were performed at null magnetic field.

- S. Haroche and F. Hartmann, Theory of saturatedabsorption line shapes, Phys. Rev. A 6, 1280 (1972).
- [2] V. S. Letokhov and V. P. Chebotaev, Nonlinear Laser Spectroscopy (Springer, Berlin, 1977).
- [3] W. Demtröder, Laser Spectroscopy: Basic Concepts and Instrumentation, 3rd ed. (Springer-Verlag, Berlin, 2003).
- [4] F. Nez, F. Biraben, R. Felder, Y. Millerioux, Optical frequency determination of the hyperfine components of the  $5S_{1/2} 5D_{3/2}$  two-photon transitions in rubidium, Opt. Commun. **102**, 432-438 (1993).
- [5] Y. Millerioux, D. Touahri, L. Hilico, A. Clairon, R. Felder, F. Biraben, and B. de Beauvoir, Towards an accurate frequency standard at  $\lambda=778\,\mathrm{nm}$  using a laser diode stabilized on a hyperfine component of the Doppler-free two-photon transitions in rubidium, Opt. Commun. 108, 91-96 (1994).
- [6] D. Touahri, O. Acef, A. Clairon, J. J. Zondy, R. Felder, L. Hilico, B. de Beauvoir, F. Biraben, and F. Nez, Frequency measurement of the 5S<sub>1/2</sub>(F = 3)-5D<sub>5/2</sub>(F = 5) two-photon transition in rubidium, Opt. Commun. 133, 471-478 (1997).
- [7] F. Biraben, The first decades of Doppler-free two-photon spectroscopy, C. R. Phys. 20, 671 (2019).
- [8] K. W. Martin, G. Phelps, N. D. Lemke, M. S. Bigelow, B. Stuhl, M. Wojcik, M. Holt, I. Coddington, M. W. Bishop, J. H. Burke, Compact Optical Atomic Clock Based on a Two-Photon Transition in Rubidium, Phys. Rev. Appl. 9, 014019 (2018).
- [9] N. D. Lemke, K. W. Martin, R. Beard, B. K. Stuhl, A. J. Metcalf and J. D. Elgin, Measurement of Optical Rubidium Clock Frequency Spanning 65 Days, Sensors 22, 1982 (2022).
- [10] R. Beard, K. W. Martin, J. D. Elgin, B. L. Kasch, and S. P. Krzyzewski, Two-photon rubidium clock detecting 776 nm fluorescence, Opt. Express 32, 7417-7425 (2024).
- [11] D. Li, K. Liu, P. Wang, and S. Kang, Dual-interrogation method for suppressing light shift in Rb 778 nm twophoton transition optical frequency standard, Opt. Express 32, 2766-2773 (2024).
- [12] K. Knabe, A. Attar, E. Barnes, H. Timmers, K. Vogel, J. Olson, A. Kortyna, G. Ycas, J. Duncan, C. Sheridan, E. Salim, APS Division of Atomic and Molecular Physics Meeting 2022, Abstract id.H11.007.
- [13] J. Olson, R. Fasano, A. Kortyna, M. Yeo, Gabriel Ycas, C. Cahall, Commercialization updates of a fielddeployable compact optical atomic clock, International Technical Meeting, Institute of Navigation, January 2024, LOng Beach, USA.
- [14] E. Ahern, J. W. Allison, C. Billington, N. Bourbeau Hébert, A. P. Hilton, E. Klantsataya, C. Locke, A. N. Luiten, M. Nelligan, R. F. Offer, C. Perella, S. K. Scholten, B. White, B. M. Sparkes, R. Beard, J. D. Elgin and K. W. Martin, Demonstration of a mobile optical clock ensemble at sea, arXiv:2406.03716v2 (2024).
- [15] J. Kitching, S. Knappe, and L. Hollberg, Miniature vaporcell atomic-frequency references, Appl. Phys. Lett. 81, 553 (2002).

- [16] R. Lutwak, A. Rashed, M. Varghese, G. Tepolt, J. Leblanc, M. Mescher, D.K. Serkland, G.M. Peake, The Miniature Atomic Clock Pre-Production Results, 2007 IEEE International Frequency Control Symposium Joint with the 21st European Frequency and Time Forum, Geneva, Switzerland, pp. 1327-1333, (2007).
- [17] S. Yanagimachi, K. Harasaka, R. Suzuki, M. Suzuki and S. Goka, Reducing frequency drift caused by light shift in coherent population trapping-based low-power atomic clocks, Appl. Phys. Lett. 116, 104102 (2020).
- [18] C. Carlé, M. Abdel Hafiz, S. Keshavarzi, R. Vicarini, N. Passilly and R. Boudot, Pulsed-CPT Cs-Ne microcell atomic clock with frequency stability below  $2\times10^{-12}$  at  $10^5$  s, Opt. Express **31**, 5, 8160-8169 (2023).
- [19] S. B. Papp, K. Beha, P. Del Haye, F. Quinlan, H. Lee, K. J. Vahala, and S. A. Diddams, Microresonator frequency comb optical clock, Optica 1, 10-14 (2014).
- [20] B. Shen, L. Chang, J. Liu, H. Wang, Q. F. Yang, C. Xiang, R. N. Wang, J. He, T. Liu, W. Xie, J. Guo, D. Kinghorn, L. Wu, Q.X. Ji, T. J. Kippenberg, K. Vahala, and J. E. Bowers, Integrated turnkey soliton microcombs, Nature 582, 365-369 (2020).
- [21] Y. Hu, M. Yu, B. Buscaino, N. Sinclair, D. Zhu, R. Cheng, A. S. Ansari, L. Shao, M. Zhang, J. M. Kahn, and M. Lončar, High-efficiency and broadband on-chip electro-optic frequency comb generators, Nat. Photon. 16, 679-685 (2022).
- [22] Y. Zhao, J. K. Jang, G. J. Beals, K. J. McNulty, X. C. Ji, Y. Okawachi, M. Lipson and A. L. Gaeta, All-optical frequency division on-chip using a single laser, Nature 627, 546-552 (2024).
- [23] Z. L. Newman, V. Maurice, T. Drake, J. R. Stone, T. C. Briles, D. T. Spencer, C. Fredrick, Q. Li, D. Westly, B. R. Ilic, B. Shen, M. G. Suh, K. Y. Yang, C. Johnson, D. M. S. Johnson, L. Hollberg, K. J. Vahala, K. Srinivasan, S. A. Diddams, J. Kitching, S. B. Papp and M. T. Hummon, Architecture for the photonic integration of an optical atomic clock, Optica 6, 680-685(2019).
- [24] V. Maurice, Z. L. Newman, S. Dickerson, M. Rivers, J. Hsiao, P. Greene, M. Mescher, J. Kitching, M. T. Hummon and C. Johnson, Miniaturized optical frequency reference for next-generation portable optical clocks, Opt. Express 28, 24708-24720 (2020).
- [25] Z. L. Newman, V. Maurice, C. Fredrick, T. Fortier, H. Leopardi, L. Hollberg, S. A. Diddams, J. Kitching and M. T. Hummon, High-performance, compact optical standard, Opt. Lett. 46, 4702-4705 (2021).
- [26] M. Callejo, A. Mursa, R. Vicarini, E. Klinger, Q. Tanguy, J. Millo, N. Passilly and R. Boudot, Short-term stability of a microcell optical reference based on Rb atom two-photon transition at 778 nm, https://arxiv.org/pdf/2407.00841 (2024).
- [27] Daniel A. Steck, Rubidium 87 D Line Data, http://steck.us/alkalidata (revision 2.2.2, 9 July 2021).
- [28] A. Szöke and A. Javan, Isotope shift and saturation behavior of the  $1.15 \mu$  transition of Ne, Phys. Rev. Lett.

- **10**, 521 (1963).
- [29] W. R. Bennett Jr., Hole burning effects in a He-Ne optical maser, Phys. Rev. 126, 580 (1962).
- [30] W. E. Lamb Jr., Theory of an optical maser, Phys. Rev. 134, A1429 (1964)
- [31] T. W. Hänsch, I. S. Shahin, and A. L. Schawlow, Highresolution saturation spectroscopy of the sodium D lines with a pulsed tunable dye Laser, Phys.Rev. Lett. 27, 707 (1971).
- [32] T. W. Hänsch, Nobel Lecture: Passion for precision, Rev. Mod. Phys. 78 (2006).
- [33] C. Wieman and T. W. Hänsch, Doppler-free laser polarization spectroscopy, Phys. Rev. Lett. 36, 1170-1173 (1976).
- [34] J. H. Shirley, Modulation transfer processes in optical heterodyne saturation spectroscopy, Opt. Lett. 7, 537(1982).
- [35] G. D. Rovera, G. Santarelli and A. Clairon, A laser diode system stabilized on the Caesium D<sub>2</sub> line, Rev. Sci. Instr. 65, 5, 1502-1505 (1994).
- [36] A. Strangfeld, S. Kanthak, M. Schiemangk, B. Wiegand, A. Wicht, A. Ling, and M. Krutzik, Prototype of a compact rubidium-based optical frequency reference for operation on nanosatellites, J. Opt. Soc. Am. B 38, 1885-1891 (2021).
- [37] A. Strangfeld, B. Wiegand, J. Kluge, M. Schoch and M. Krutzik, Compact plug and play optical frequency reference device based on Doppler-free spectroscopy of rubidium vapor, Opt. Express 30, 12039 (2022).
- [38] J. S. Torrance, B. M. Sparkes, L. D. Turner, and R. E. Scholten, Sub-kilohertz laser linewidth narrowing using polarization spectroscopy, Opt. Express 24, 11396 (2016).
- [39] S. Lee, S.-B. Lee, S. E. Park, H.-G. Hong, M.-S. Heo, S. Seo, J. Jeong, T. Y. Kwon, and G. Moon, Compact modulation transfer spectroscopy module for highly stable laser frequency, Opt. Lasers Eng. 146, 106698 (2021).
- [40] H. Shang, T. Zhang, J. Miao, T. Shi, D. Pan, X. Zhao, Q. Wei, L. Yang, and J. Chen, Laser with 10<sup>-13</sup> short-term instability for compact optically pumped cesium beam atomic clock, Opt. Express 28, 6868 (2020).
- [41] J. Miao, T. Shi, J. Zhang and J. Chen, Compact 459 nm Cs cell optical frequency standard with  $2.1 \times 10^{-13} / \sqrt{\tau}$  short-term stability, Phys. Rev. Appl. 18, 024034 (2022).
- [42] S. Lee, G. Moon, S. Eon Park, H.-G. Hong, J. H. Lee, S. Seo, T. Y. Kwon, and S.-B. Lee, Laser frequency stabilization in the  $10^{-14}$  range via optimized modulation transfer spectroscopy on the  $^{87}$ Rb  $D_2$  line, Opt. Lett. 48, 1020-1023 (2023).
- [43] T. Schuldt, K. Döringshoff, E. V. Kovalchuk, A. Keet-

- man, J. Pahl, A. Peters and C. Braxmaier, Development of a compact optical absolute frequency reference for space with  $10^{-15}$  instability, Appl. Opt. **56**, 1101 (2017).
- [44] Z. Zhang, Z. Wang, H. Liu, W. Yuan, W. You, J. Zhang, K. Deng and Z. Lu, An ultra-stable laser based on molecular iodine with a short-term instability of 3.3 × 10<sup>15</sup> for space based gravity missions, Classical and Quantum Gravity 40, 225001 (2023).
- [45] J. D. Roslund, A. Cingoz, W. D. Lunden, G. B. Partridge, A. S. Kowligy, F. Roller, D. B. Sheredy, G. E. Skulason, J. P. Song, J. R. Abo-Shaeer and M. M. Boyd, Optical clocks at sea, Nature 628, 736-740 (2024).
- [46] M. Abdel Hafiz, G. Coget, E. de Clercq and R. Boudot, Doppler-free spectroscopy on the Cs D<sub>1</sub> line with a dualfrequency laser, Opt. Lett. 41, 2982 (2016).
- [47] M. Abdel Hafiz, D. Brazhnikov, G. Coget, A. Taichenachev, V. Yudin, E. de Clercq, and R. Boudot, High-contrast sub-Doppler absorption spikes in a hot atomic vapor cell exposed to a dual-frequency laser field, New J. Phys. 19, 073028 (2017).
- [48] D. Brazhnikov, M. Petersen, G. Coget, N. Passilly, V. Maurice, C. Gorecki and R. Boudot, Dual-frequency sub-Doppler spectroscopy: Extended theoretical model and microcell-based experiments, Phys. Rev. A 99, 062508 (2019).
- [49] A. Gusching, J. Millo, I. Ryger, R. Vicarini, M. Abdel Hafiz, N. Passilly, and R. Boudot, Cs microcell optical reference with frequency stability in the low 10<sup>-13</sup> range at 1 s, Opt. Lett. 48, 1526-1529 (2023).
- [50] M. Zhao, X. Jiang, R. Fang, Y. Qiu, Z. Ma, C. Han, B. Lu, and C. Lee, Laser frequency stabilization via bichromatic Doppler-free spectroscopy of an  $^{87}$ Rb  $D_1$  line, Appl. Opt. **60**, 17, 5203-5207 (2021).
- [51] G. Moon and H. R. Noh, Analytic solutions for the saturated absorption spectra, J. Opt. Soc. Am. B 25, 701-711 (2008).
- [52] A. Gusching, M. Petersen, N. Passilly, D. Brazhnikov, M. Abdel Hafiz, and R. Boudot, Short-term stability of Cs microcell-stabilized lasers using dual-frequency sub-Doppler spectroscopy, J. Opt. Soc. Am. B 38, 3254 (2021).
- [53] G. Moon and H.-R. Noh, Analytic calculation of linear susceptibility in velocity-dependent pump-probe spectroscopy, Phys. Rev. A 78, 032506 (2008).
- [54] S. Li, B.Wang, X. Yang, Y. Han, H.Wang, M. Xiao, and K. C. Peng, Controlled polarization rotation of an optical field in multi-Zeeman-sublevel atoms, Phys. Rev. A 74, 033821 (2006).
- [55] H.-R. Noh, W. Jhe, Analytic solutions of the susceptibility for Doppler-broadened two-level atoms, Optics Communications 283, 2845-2848 (2010).

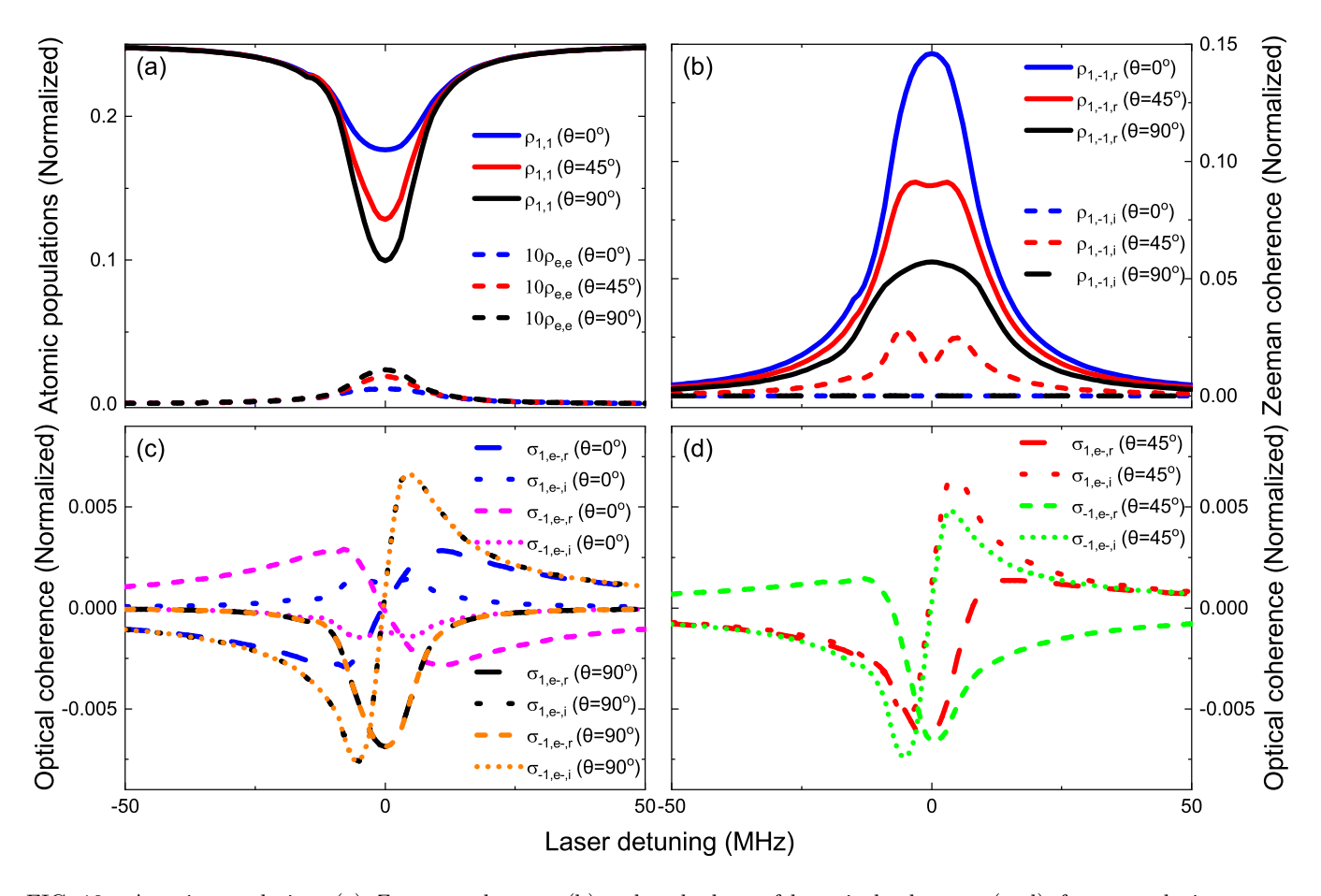


FIG. 10. Atomic populations (a), Zeeman coherence (b) and probe beam felt optical coherence (c, d), for zero velocity atoms, as function of the laser detuning, at various polarization angles.

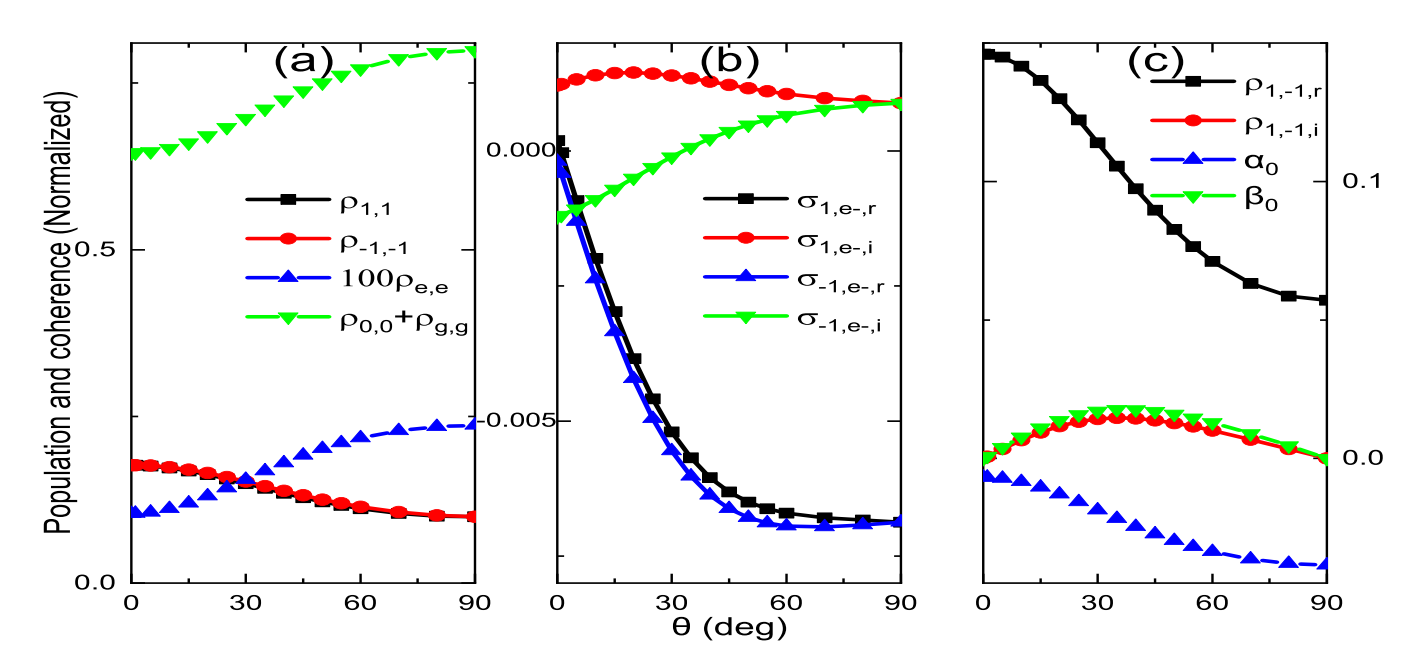


FIG. 11. Atomic populations (a), probe beam felt optical coherence (b), Zeeman coherence,  $\alpha_0$  and  $\beta_0$  (c), for zero-velocity atoms and null laser detunings ( $\Delta_+ = \Delta_- = 0$ ), versus the polarization angle  $\theta$ .

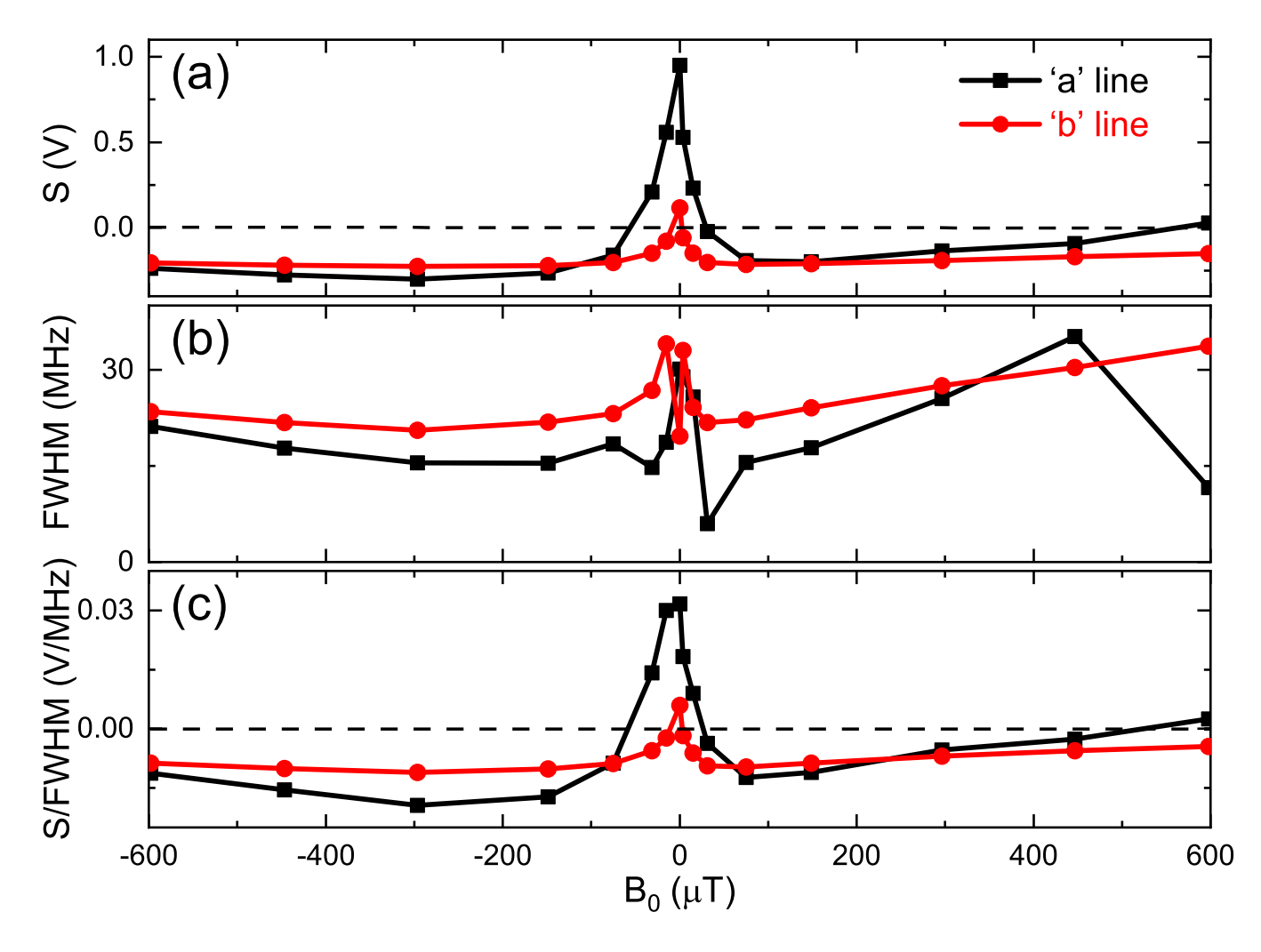


FIG. 12. Signal (a), linewidth (b) and S/FWHM ratio (c) of 'a' and 'b' lines versus the static magnetic field ( $B_0$ ). Experimental parameters are:  $T_{cell} = 40$  °C,  $\theta = -45$ °,  $P_{pump} = 100 \,\mu\text{W}$ .